Effects of Particle Diameter and Coke Layer Thickness on Solid Flow and Stress Distribution in BF by 3D Discrete Element Method

DEREJE DEGEFA GELETA and JOONHO LEE

In order to reduce ironmaking-related CO_2 emissions, hydrogen-enriched blast furnace (BF) operation is currently under development. In hydrogen-enriched BF operation, coke layer thickness can be decreased to reduce CO_2 emissions. However, BFs operating with thin coke layers may experience instability or discontinuous phenomena such as particle slip and gas channeling problems, so it is important to optimize the particle diameter and coke layer thickness for optimal BF operation. In this study, the effects of particle diameter and coke layer thickness on the solid flow and stress distribution in a BF were analyzed using a three-dimensional discrete element method. Furthermore, the effects of particle diameter and coke layer thickness on the burden layer stabilities, particle velocities, and particle stress distributions have been investigated. The results show that decreasing the coke layer thickness caused instability owing to the mixing of the coke and ore layers in the BF-cohesive zone and slight increases in both the average particle velocities and the average normal particle stress magnitudes. In addition, the average particle velocities and average normal particle stresses were higher for the smaller particles than for the larger ones during the simulations.

https://doi.org/10.1007/s11663-018-1368-7

I. INTRODUCTION

A blast furnace (BF) is a complex counter-current reactor involving numerous physical processes, among which heat transfer, thermodynamics, chemical reactions, and solid and fluid transports are the major ones. However, high temperatures and pressures in BFs complicate dissection studies, *in situ* measurements, and physical experiments. Consequently, computer simulations have played a very important role in understanding the intricate phenomena occurring inside BFs.[1–13]

In BFs, alternating charges of coke and ore form the burden layers. Coke serves as a heat source to melt iron ore,[14] a carbon source to carburize iron,[15,16] a reducing agent generating carbon monoxide,[14,17] and a means of developing permeability for gas flows.[18–22] Indeed, iron and steel manufacturers have been targeting reductions in the amounts of coke they consume to minimize production costs and carbon dioxide emissions by developing technologies such as hydrogen-enriched ironmaking.[23–26] However, minimizing coke consumption may result in thin coke layers, which in turn may lead to unstable situations such as the mixing of burden materials, yielding gas channeling problems, which greatly affect heat transfer from gas to solid burden and consequently decrease BF efficiency.

Gas permeabilities, which may affect BF efficiencies, rely not only on burden layer thicknesses but also on particle shapes and diameters.[1,20] The average particle diameters of the coke and ore used as raw materials in BFs are in the ranges 45 to 55 and 15 to 25 mm, respectively.[27] Owing to this difference in diameters, the permeability of coke is five times greater than that of the ore. Therefore, it is essential to understand gas permeability in thinner coke layers.

Currently, many iron and steel manufacturers use 5600-m^3 or larger BFs to increase energy efficiency.[22,23] Increasing BF volume, however, disturbs the burden layer arrangements, average normal particle stresses, and particle velocity distributions, especially in the lower parts of BFs.[28] Several researchers have applied numerical simulations such as continuum computational fluid dynamics (CCFD)[29,30] and discrete element method (DEM)[31–33] models to BF studies. In recent years, DEM and CFD have even been coupled.[1,34–46] For example, Fan *et al.*[47] employed DEM using burden layer arrangement, particle velocity, and stress distribution as parameters to investigate the effect of cohesion-zone shape on solid flow. Jiang-Liang *et al.*[48] used the same parameters to analyze the impacts of BF

DEREJE DEGEFA GELETA and JOONHO LEE are with the Department of Materials Science and Engineering, Korea University, 145 Anam-ro, Seongbuk-gu, Seoul 136-713, Korea. Contact e-mail: joonholee@korea.ac.kr

Manuscript submitted March 26, 2018.
Article published online August 1, 2018.

profiles such as shaft and bosh angles on burden flow. Natsui *et al.*[43,49,50] also studied the distributions of particle velocity, stress, drag, and pressure in BFs by applying the same technique. Keyser *et al.*[51] used the continuum approach to investigate the effect of coal particle diameter on the packed bed pressure loss and gas flow distribution.

Based on these previous studies, it is concluded that numerical simulations for the hydrogen-enhanced operation of BFs may give insight into the direction of practical operation, particularly into how to maintain stable gas permeability through the burden layers with less coke charging in a hydrogen-enhanced environment. Above the cohesive zone, when the different diameter coke and ore particles are mixed, the smaller particles occupy the free space between larger ones and minimize gas permeability. Among the factors that cause degradation of coke in packed bed, some of them are solution loss reaction, shuttering, and abrasion. Here, abrasion is caused by stress developed due to contact forces. The abraded particles and the generated fine particles reduce the gas permeability in the packed bed. In addition, the abrasion of coke particles can be reduced by increasing the particle velocity. If the burden flows faster, the collision of particles will be minimized and possibly create lower stress field in the stress network area. Then, lower stress field mitigates abrasion and enhances permeability. Therefore, the information of stress distribution and particle velocity variation are important to understand the behavior in BF.

The aims of the present study are to investigate the effects of particle diameter and coke layer thickness on the burden layer arrangement, average particle velocity, and normal particle stress distribution in the entire BF. Natsui *et al.*[41,43] showed that the effects of gas flows on the burden layer arrangements, average particle velocities, and normal particle stress distributions in BFs by coupling DEM and CFD, and concluded that there were slight effect but the general trend could be explained by DEM simulation. Therefore, three-dimensional DEM is adequate for examining these objectives because it can determine how thin coke layers can enhance the molten iron production rate while reducing coke consumption and the corresponding carbon dioxide emissions without affecting BF stability.

II. MODEL DESCRIPTION

A. *Fundamental Equations of DEM*

DEM is an analytical method based on Newton's second law of motion for translational and rotational motions of particles.[31,49,52] The particle positions, velocities, and accelerations are calculated based on discrete time for all the particles in the control volume under consideration. The contact force between particles or between a particle and a wall is composed of elastic and damping forces in both the normal and tangential directions. In this study, we implemented the built-in Hertz–Mindlin no-slip contact model of the EDEM commercial software.[1,53,54] Schematics of the DEM model and the interactive forces between particles *i* and *j* are shown in Figures 1(a) and (b) respectively. The model consists of a slider to represent friction, a dash pot to indicate damping, and a spring for the elastic force in both directions. The fundamental equations that govern the motions of particles are given by Eqs. [1] and [2][1,46,52,55] for translation and rotation, respectively:

$$m_i \frac{\mathrm{d}^2 \boldsymbol{u}_i}{\mathrm{d}t^2} + \eta \frac{\mathrm{d}\boldsymbol{u}_i}{\mathrm{d}t} + K\boldsymbol{u}_i + m_i \boldsymbol{g} = 0 \qquad [1]$$

$$I_i \frac{\mathrm{d}^2 \boldsymbol{\varphi}_i}{\mathrm{d}t^2} + \eta R_i^2 \frac{\mathrm{d}\boldsymbol{\varphi}_i}{\mathrm{d}t} + K R_i^2 \varphi_i = 0, \qquad [2]$$

where m, K, η, $\mathbf{g}$, I, $\boldsymbol{u}_i$, $\boldsymbol{\varphi}_i$, and R denote the mass, spring stiffness, damping coefficient, gravitational acceleration, moment of inertia, translational displacement, angular displacement, and radius of particle i respectively. The contact forces, $\boldsymbol{F}_n$ and $\boldsymbol{F}_t$, in the normal and tangential directions, respectively, acting on particle *i* by particle *j* can be derived as follows:

$$\boldsymbol{F}_n = \left[K_n \Delta \boldsymbol{u}_{n,ij} + \eta_n \frac{\Delta \boldsymbol{u}_{n,ij}}{\Delta t} \right] n_{ij} \qquad [3]$$

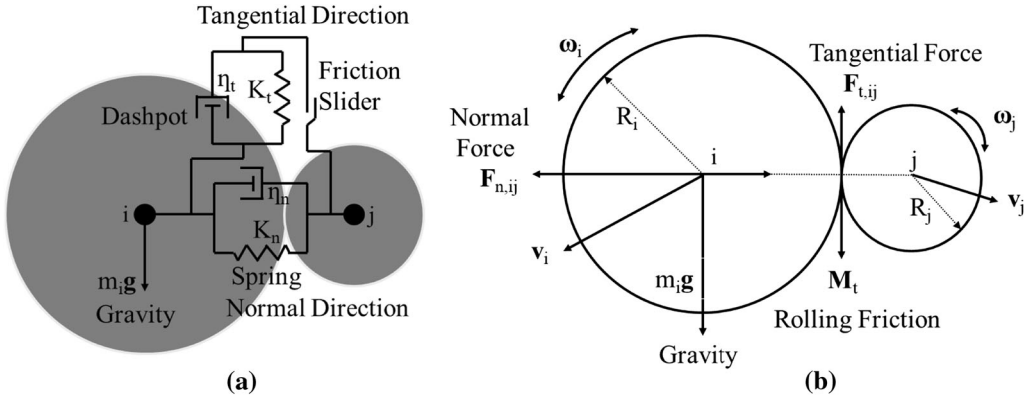

Fig. 1—(*a*) Contact model in DEM. (*b*) Interactive forces between particles *i* and *j*.

$$\boldsymbol{F}_t = \left[K_t\left(\Delta \boldsymbol{u}_{t,ij} + \varphi_{ij}\right) + \eta_t \frac{\left(\Delta \boldsymbol{u}_{t,ij} + \varphi_{ij}\right)}{\Delta t} \right] t_{ij}, \quad [4]$$

where Δu_{ij} and $\Delta \phi_{ij}$ represent the linear and angular displacements of the particle centroids, and n_{ij} and t_{ij} are the unit vectors in the normal and tangential directions, respectively. Subscripts n and t denote the normal and tangential directions, respectively. Spring stiffness, K and damping coefficient, η are determined from particle properties such as the Young's modulus (E), Poisson's ratio (υ), contact-circle radius (R), and mass (m) as follows:

$$K_n = 2R\left(\frac{1-\upsilon_i^2}{E_i} + \left(\frac{1-\upsilon_j^2}{Ej}\right)\right) \quad [5]$$

$$K_t = 8R\left(\frac{2(2-\upsilon_i)(1+\upsilon_i)}{E_i} + \frac{2\left(2-\upsilon_j\right)(1+\upsilon j)}{E_j}\right) \quad [6]$$

$$\eta_n = 2\sqrt{mK_n} \quad [7]$$

$$\eta_t = 2\sqrt{mK_t} \quad [8]$$

The Coulomb friction forces, $\boldsymbol{F}_{t,ij}$ and rolling friction torques, $\boldsymbol{M}_t$ opposing the rotations are given by:

$$\boldsymbol{F}_{t,ij} = \mu\left|\boldsymbol{F}_{n,ij}\right| \quad [9]$$

$$\boldsymbol{M}_t = \frac{3}{8}\alpha R|\boldsymbol{F}_n|, \quad [10]$$

where μ and α are static and rolling friction coefficients, respectively. The torque $\boldsymbol{T}$ generated by tangential forces is calculated as:

$$\boldsymbol{T} = R\sum \boldsymbol{F}_t, \quad [11]$$

where $\sum \boldsymbol{F}_t$ is the summation of forces in tangential direction from Eqs. [4] and [9]. In Figure 1(b), v_i and v_j are the translational and ω_i and ω_j are the rotational velocities of particles i and j, respectively. The detailed descriptions of the DEM equations can be found in the studies of Natsui *et al.*[43,44,56,57]

III. SIMULATION CONDITIONS

In the simulations, two different-sized BFs were employed. The effects of coke layer thickness on solid flow and stress distribution were investigated with a BF whose inner volume was 5775 m^3 and which had 40 tuyères. The effects of particle diameter on solid flow and stress distribution were investigated with a BF whose inner volume was 1344 m^3 and which had 24 tuyères. The volume of the latter one was roughly two-thirds that of the former one. Owing to computational difficulties, only one-quarter and one-sixth of the revolutions were considered in the cases of the effects of coke layer thickness and the effects of particle diameter respectively. The sectioning wall was assumed frictionless, and the images reported in this paper were taken at the middle of the control volume of the simulation to remove the possible effect of the frictionless sectioning wall. The schematic diagram of the BF is shown in Figure 2(a) and the geometric dimensions of the control volumes are listed in Table I. The calculation region was approximated by dividing it into rectangular-coordinate tetrahedrons, as shown in Figure 2(b). To analyze the effects of particle diameter on solid flow and stress distribution, two cases were considered by changing the coke and iron ore particle diameters from 0.3 and 0.15 to 0.15 and 0.075 m, respectively, as listed in Table II. Likewise, to analyze the effects of coke layer thickness on solid flow and stress distribution, three cases were considered by varying the particle layer thicknesses, *i.e.*, by changing the number of particles per layer, as listed in

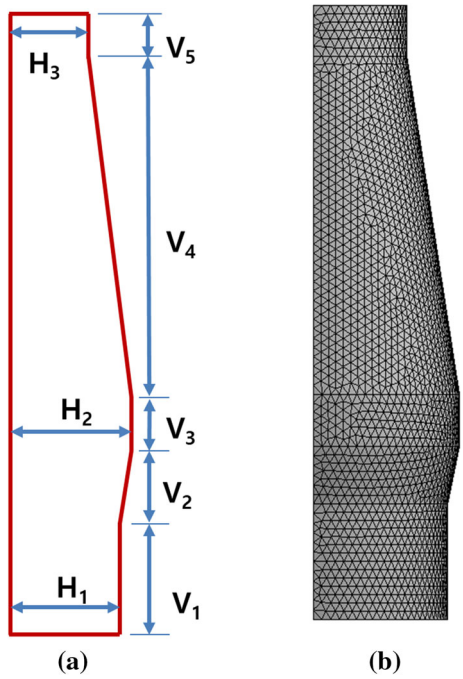

Fig. 2—Schematics of (*a*) blast furnace geometry and (*b*) computational grid for DEM.

Table I. Dimensions of Blast Furnace Control Volumes

Inner Volume (m^3)	5775	1344
Number of Tuyères	40	24
H1 (m)	7.8	5.0
H2 (m)	8.6	5.7
H3 (m)	5.6	3.6
V1 (m)	5.5	3.4
V2 (m)	4	3.4
V3 (m)	3	3.4
V4 (m)	19	10
V5 (m)	2	2
Revolution Angle (deg)	90	60

Table II. Calculation Parameters Used in DEM Analysis

Parameters	Layer Thickness			Particle Size			
	Coke	Ore	Wall		Coke	Ore	Wall
Particle Diameter (m)	0.3[43]	0.15[43]		case 1	0.3	0.15	
				case 2	0.15	0.075	
Coefficient of Restitution[1]	0.5	0.5	0.5		0.3	0.3	0.3
Static Coefficient of Friction[43]	1	1	0.7		1	1	0.7
Rolling Coefficient of Friction[43]	2.5	1.25			2.4	1.25	
Apparent Density (kg/m^3)[43]	1100	4000			1100	4000	
Young's Modulus (GPa)[43]	1	1	2		1	1	2
Poisson's Ratio[43]	0.21	0.24	0.3		0.21	0.24	0.3
Time Step (s)	1.6×10^{-5}				1.25×10^{-4}		

Table III. Number of Particles Per Layer for Analysis of Layer Thickness in DEM

Case	Coke	Ore	Ore/Coke
a	1000	11,000	11
b	1300	11,000	8.64
c	1300	14,300	11

Table III. In case (a), the numbers of charged coke and ore particles were roughly adjusted so that the thicknesses of the coke and ore layers were equal to the diameters of 1 coke and 3 ore particles, respectively, if orderly arranged in the BF-cohesive zone. In case (b), the coke layer thickness was increased while the ore layer thickness was kept constant. Thus, the ratio of ore to coke per layer was decreased from 11 to 8.64. In case (c), the iron ore layer thickness was increased again to produce the same ore-to-coke ratio as in case (a).

Spherical particles were assumed in the simulations. To accelerate the calculations, the particle diameters were proportionally enlarged. The particle properties and simulation conditions, listed in Table II, were taken from previous studies.[43] Most of the physical properties were obtained from Reference 43. Here, higher static and rolling friction coefficients for the contact forces between particles and between particles and the BF wall were employed to take into consideration particle shape factors. The value of coefficient of restitution was taken from a value in the range of 0.2 to 0.6 suggested in Reference 1 to form a stable layer on the top. The coke particles were discharged from the raceway due to gravitational force of its own weight through the holes of the tuyeres naturally. The diameter of a tuyere hole was taken as 1 m. Tuyeres were uniformly distributed around the circumference.

IV. RESULTS AND DISCUSSION

A. *Effects of Coke Layer Thickness on Solid Flow and Stress Distribution*

1. *Burden layer arrangements*

Initially, the BF was filled to the throat with coke particles alone. As the coke particles were discharged from the raceway, representing their consumption, iron ore and coke particles were alternately charged from the throat to maintain the stoke line at a fixed level, so that a steady solid flow was maintained. As a result, a multilayer consisting of a sequence of alternating iron ore and coke particle layers was formed, as shown in Figures 3(a) through (c), where red and green represent the iron ore and coke particles, respectively.

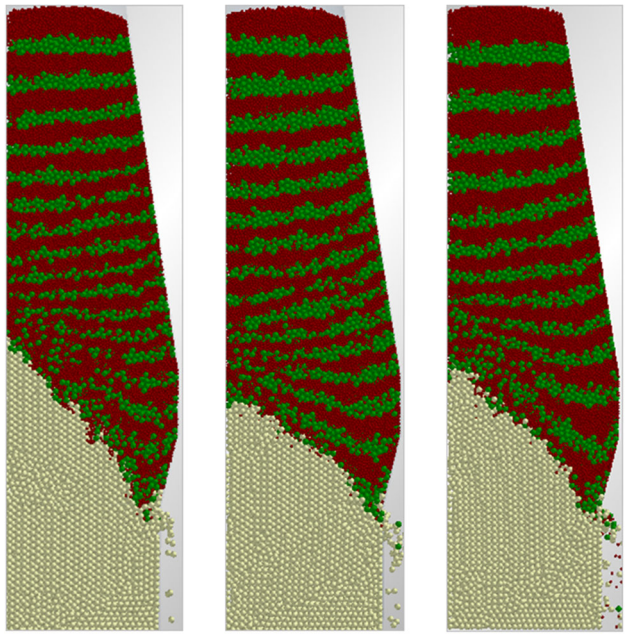

Fig. 3—DEM simulation results. Green and red represent coke and iron ore particles, respectively. (*a*) 1000 coke and 11,000 ore particles, (*b*) 1300 coke and 11,000 ore particles, and (*c*) 1300 coke and 14,300 ore particles per layer.

The effects of the coke layer thickness on the solid flow and stress distribution can be clearly observed by measuring many parameters such as the stability of the layers in the lower part of the BF, the height of deadman, the particle descending velocity, and the stress distribution. The burden layers indicated in Figures 3(a) through (c) were formed by varying the number of coke and iron ore particles per layer introduced into the BF. The exact number of particles per layer and their relative ratios are listed in Table III. In all three cases, despite the variation in layer thickness, separate layers were formed in the upper part of the BF. As the particles descended, the layers became thinner in the BF-cohesive

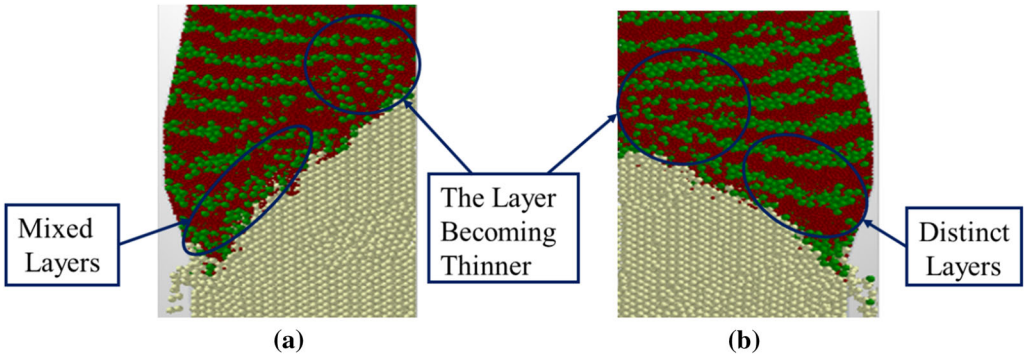

Fig. 4—Comparison of layers described in Fig. 3 considering only the lower part of BF. Green and red represent coke and iron ore particles, respectively. (*a*) 1000 coke and 11,000 ore particles, and (*b*) 1300 coke and 11,000 ore particles per layer.

zone. With the increasing ore-to-coke particle ratio for a relatively thin coke layer, as in case (a), the coke and ore layers became increasingly mixed and unstable in the lower part of the BF, which may negatively affect the gas permeability in the BF. In cases (b) and (c), on the other hand, distinct layers were formed with the increasing coke layer thickness, irrespective of the ore-to-coke particle ratio, as shown in Figures 4(a) and (b). Here, the deadman height seemed to depend on the ore-to-coke particle ratio rather than on the coke layer thickness.

The deadman, which served as the coke supply source for combustion, is the conical deposit of coke particles in the lower part of the BF just below the cohesive zone,[58] as represented by the light gray particles in Figures 3 and 4. As per the DEM calculations, the deadman heights above the tuyère level were around 8, 5.6, and 7 m in cases of (a), (b), and (c), respectively, suggesting that decreasing the coke layer thickness increased the instability in the lower part of the BF. In addition, reducing the overall coke consumption rate would increase the deadman height. In Figures 3 and 4, it took 641.4, 436.3, and 425.6 seconds of simulation time to form the layers in (a), (b), and (c) cases, respectively.

2. *Normal stresses*

Owing to interparticle collisions and collisions between particles and the BF wall, descending particles are subjected to contact forces. Increased stress during BF operation may increase dust generation, which may prevent the formation of permeable channels for gas flow. Therefore, the effect of the coke consumption rate on the normal stress should be investigated. The average normal stress developed on an individual particle was determined by dividing the resultant of all the forces acting on the particle by its surface area. Thus, the normal stress, $\boldsymbol{\sigma}_n$, on each particle was calculated by[37,43,47,48]

$$\boldsymbol{\sigma}_n = \sum_j \boldsymbol{F}_{n,ij} \Big/ \pi d_i^2 \qquad [12]$$

where d_i is the diameter of particle i, and $\boldsymbol{F}_{n,ij}$ is the normal force applied by either particle j or the wall on particle i.

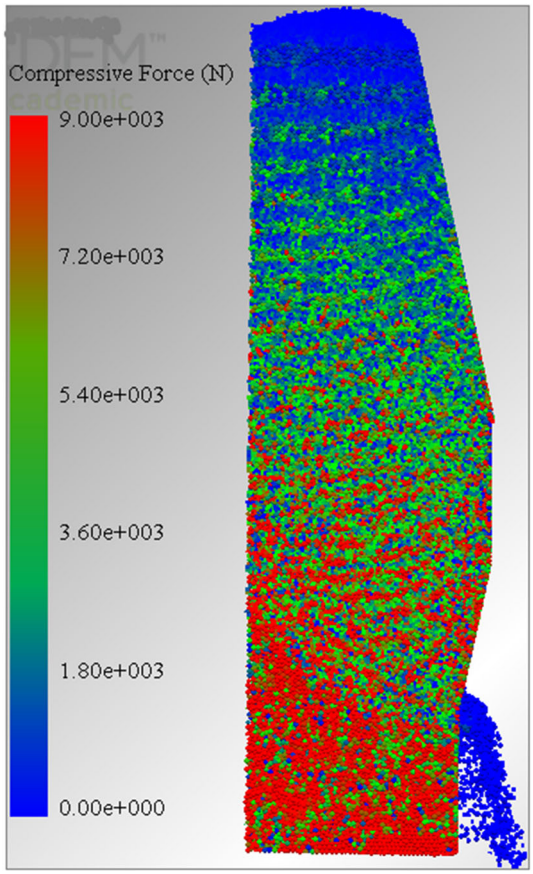

Fig. 5—Normal force distribution for steady descent in case (c).

A typical normal force distribution in the whole BF is shown for case (c) in Figure 5. The high and low normal forces are indicated in red and blue, respectively. The distribution shows that higher normal forces were developed on the particles in the lower part of the BF because particles descending from above applied more pressure on the particles below owing to gravity. As indicated in blue in Figure 5, the particles in the upper part of the BF were subjected to the minimum average normal force. The particles at the raceway clearly were subjected to lower average normal forces than the

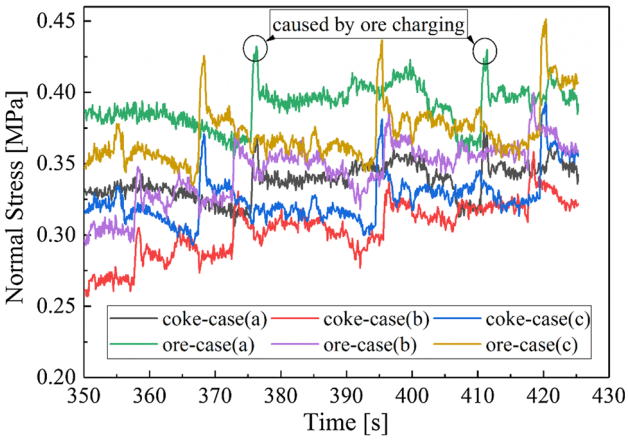

Fig. 6—Effect of layer thickness on average normal stresses on particles in blast furnace.

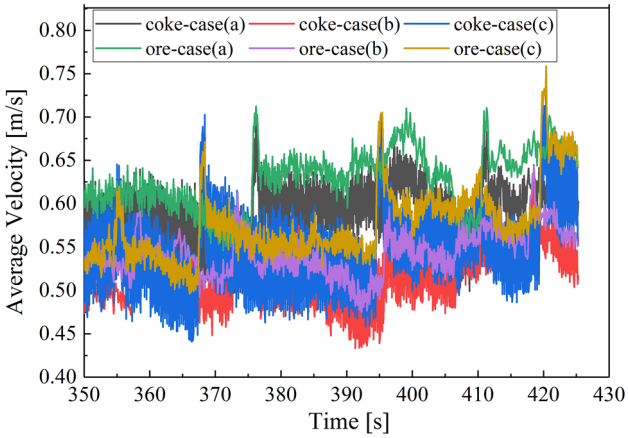

Fig. 7—Effect of layer thickness on average velocities of particles in blast furnace.

nearby particles in the lower part of the BF. The particles in the deadman, on the other hand, were subjected to the maximum normal force.

To investigate the effect of coke layer thickness on normal particle stress distribution, variations in the average normal particle stress over time are shown in Figure 6. The six graphs in Figure 6 represent the average normal stresses on the iron ore and coke particles in cases (a), (b), and (c). The normal stresses developed on both the iron ore and coke particles gradually increased over time, and the iron ore particles developed higher normal stresses than the coke particles in all cases. The highest normal stress was developed on the iron ore particles in case (a) when the coke layer thickness was the minimum and the ore-to-coke particle ratio was high. In contrast, the lowest normal stress was developed on the coke particles in case (b) when the coke layer thickness was the maximum and the ore-to-coke particle ratio was low. Zhang *et al.* reported that higher average normal stresses, as shown in case (a), caused wall abrasion, especially in the lower parts of BFs.[48] It is noteworthy that while maintaining a constant coke layer thickness as the ore layer thickness was increased, as shown in case (c), the average normal stress could be decreased.

3. *Average particle velocities*

Figure 7 shows the average velocities of the coke and ore particles in the BF over time for cases (a), (b), and (c). In all the graphs, the average particle velocities were roughly constant except for the intermittent high velocity peaks and the small fluctuations in particle velocity between them. The average particle velocity was higher in case (a) when the ore-to-coke particle ratio was the maximum and the coke layer was relatively thin, corresponding to exactly when the normal stress was the maximum. The average particle velocity was lower, corresponding to exactly when the normal stress was the minimum, in case (b). Therefore, it seemed that the thinner the coke layer, the faster the particles descended. The average particle velocity slightly increased when a constant coke layer thickness was maintained, while the ore layer thickness was increased. Consequently, it is expected that in ironmaking BF, the molten iron production rate can be accelerated by decreasing the coke's consumption rate. However, since burden motion is not a rate-limiting step in a real process, reduction, carburization, and melt formation should be accelerated simultaneously.

B. *Effects of Particle Diameter on Solid Flow and Stress Distribution*

1. *Burden layer arrangements*

To investigate the effects of particle diameter on solid flow and stress distribution, two cases in which the coke particle diameter was twice the iron ore particle diameter were compared for large and small particles. The simulation burden layer patterns are shown in Figures 8(a) and (b). For the smaller particles, as shown in Figure 8(b), the burden layers were more stable and ordered, even in the lower part of the BF. Obviously, more burden layers were needed to fill the BF, and a short deadman was formed. The smaller particles, especially those in the lower part of the BF, also showed the microscopic effects of collision with the BF wall. The larger particles, on the other hand, showed some layer disruption in the lower part of the BF, as shown in Figure 8(a). The BF was filled with fewer burden layers, and the height of the deadman was increased. As per the DEM calculations, the deadman heights above the tuyère were around 4.58 and 1.77 m for the larger and smaller particles, respectively, suggesting that increasing the particle diameter to enhance the gas permeability may yield instability in the lower parts of BFs operating under hydrogen-enhanced conditions. It took 471.31 and 153.7 seconds of simulation time to form the layers in (a) and (b) cases of Figure 8, respectively.

2. *Normal stresses*

The variations in the average normal stresses of the particles over time are shown in Figure 9. The average normal stresses developing on the large and small coke and iron ore particles gradually increased over time, as

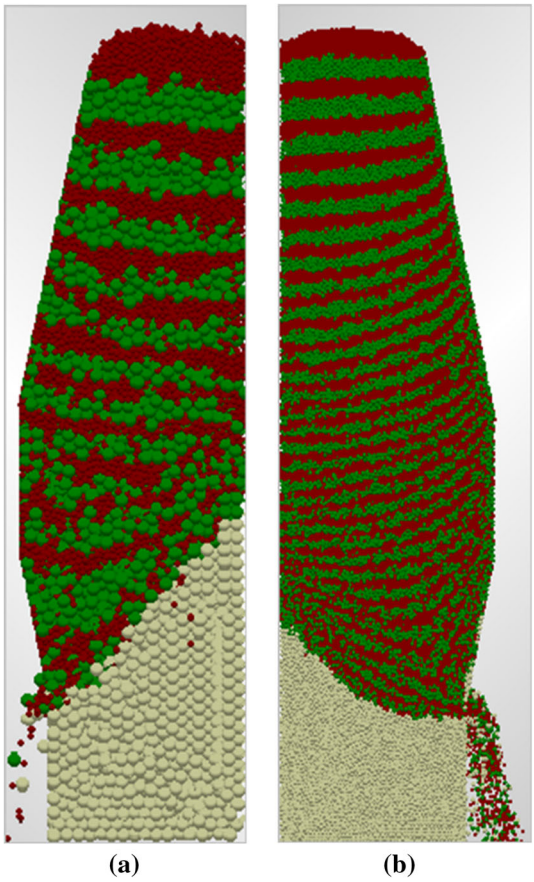

Fig. 8—DEM simulation results for effects of particle diameters on solid flow and stress distribution. Green and red represent coke and iron ore particles, respectively. (*a*) Coke and iron ore particle diameters = 0.3 and 0.15 m, respectively; 600 coke and 3600 iron ore particles per layer. (*b*) Coke and iron ore particle diameters = 0.15 and 0.075 m, respectively; 5000 coke and 13,000 iron ore particles per layer.

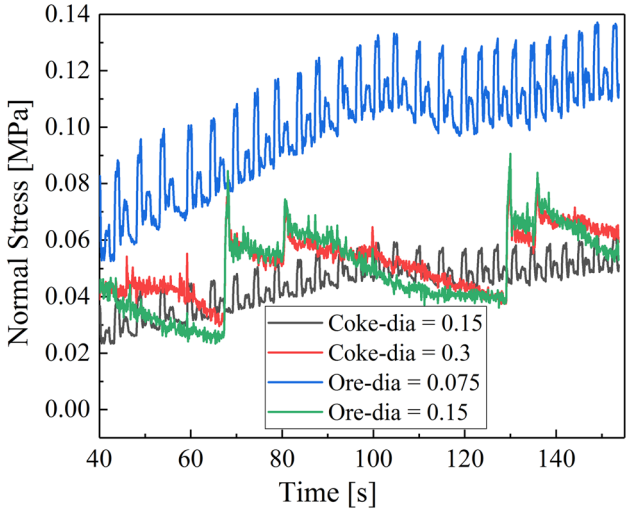

Fig. 9—Effects of particle diameter sizes on average normal stresses of particles in blast furnace.

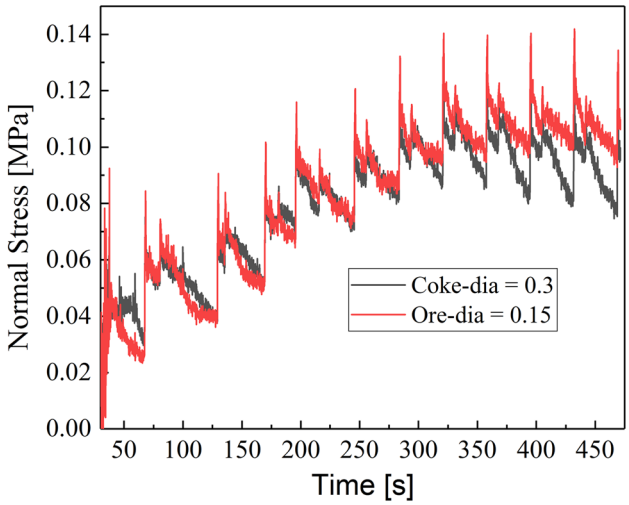

Fig. 10—Distributions of average normal stresses among coke and ore particles.

in the burden layer thickness simulations discussed in Section IV–A–2. The smaller particles were subjected to higher normal stresses than the larger ones owing to the higher packing density of the smaller particles, and the iron ore particles were subjected to higher normal stresses than the coke particles. However, the overall trend was slightly different for the larger particles, as shown in Figure 10. Early in the simulation, owing to layer mixing and instability, the larger iron ore particles seemed to be more stable than the larger coke ones, and the larger coke particles were subjected to higher normal stresses. As a result, the average normal stress developed on the larger coke particles was slightly higher than that developed on the larger iron ore ones except when the iron ore and coke were charged. However, the larger particles stabilized over time, and the normal stress developed on the larger iron ore particles became higher than that developed on the larger coke particles starting from around 300 seconds. Figure 11 compares the average normal stresses developed on the large (dia = 0.3 m) and small (dia = 0.15 m) coke particles. The periodic tall peaks were generated when the iron ore was charged. The periodic medium peaks between the tall peaks were generated when the coke was charged. The periodic small peaks between the medium peaks were generated by the interparticle collisions and slipping motions of the descending particles. The difference between the peak heights when the iron ore and coke were charged was attributed to the difference in the particle densities. In the simulation for the large particles, the gaps between the periodic tall peaks, representing the iron ore charging intervals, were large, indicating that the larger particles took more time than the smaller ones to accumulate even a single particle layer in the simulations.

3. *Average particle velocities*

The average particle velocities showed steady particle flows, which is almost the same trend as that shown by the layer thicknesses. The velocity distributions of the large- and small-diameter coke and iron ore particles are presented in Figure 12. Clearly, the average velocities of

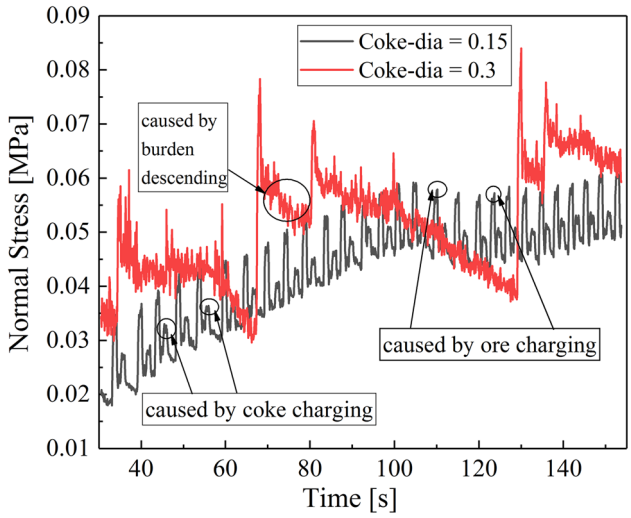

Fig. 11—Distributions of average normal stresses among coke particles.

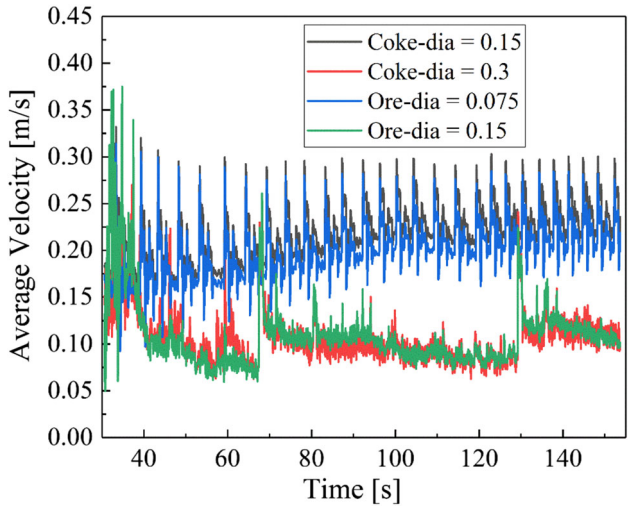

Fig. 12—Effects of particle sizes on average velocities of particles in blast furnace.

the smaller particles were higher than those of the larger ones during the simulations, suggesting that increasing the diameters of the particles in BFs may reduce molten metal production rates. However, as mentioned in Section IV–A–3 in a real process, reduction, carburization and melt formation should be accelerated to increase the production rate.

V. CONCLUSIONS

In this study, a three-dimensional discrete element method was used to analyze the coke and iron ore particle flows in a BF for operations. The effects of particle diameter and coke layer thickness on the solid flow and stress distribution in a BF were demonstrated by calculating parameters such as burden layer arrangements, average particle velocities, and normal particle stress distributions for large and small coke and iron ore particles and for three different coke layer thicknesses.

The particles were subjected to the highest average normal stress in case (a) when the ore-to-coke particle ratio was the highest and the coke layer was relatively thin. The particles were subjected to the lowest average normal stress in case (b) when the ore-to-coke particle ratio was the lowest and the coke layer was thicker. In case (c), the particles were subjected to average normal stress between those to which the particles in cases (a) and (b) were subjected when the ore-to-coke particle ratio was the highest and the number of coke particles per layer was the same as that in case (a). The highest average particle velocity was obtained when the ore-to-coke particle ratio was the highest and the coke layer was relatively thin, exactly when the normal stress was the highest. Therefore, the thinner the coke layer, the faster the burden layers descended. However, thinner coke layers may lead to instability and layer mixing in the BF-cohesive zone. Consequently, case (c) showed the optimal reactor operating conditions because the burden layers descended quickly, and the particles were subjected to average normal stresses, while distinct coke and iron ore layers were formed.

The average normal particle stress increased over time owing to more interparticle collisions as more particles were introduced into the BF. The smaller particles were subjected to higher average normal stresses than the larger ones during the simulations. All the particles steadily descended apart from the small fluctuations in particle velocity observed when the iron ore and coke were charged. During the simulations, the smaller particles showed higher average velocities than the larger ones, suggesting that operating BFs with larger-diameter particles may enhance gas permeability, which may decrease the molten iron production rate.

ACKNOWLEDGMENTS

This study was supported by the Industrial Strategic Technology Development Program (20172010106300, Development of Hybrid ironmaking processes for lower CO_2 emissions) funded by the Ministry of Trade, Industry & Energy (MOTIE, Korea). The authors are grateful to Assistant Professor Shungo Natsui at Hokkaido University for his informative discussion.

REFERENCES

1. A. Adema, Y. Yang, and R. Boom: *ISIJ Int.*, 2010, vol. 50, pp. 954–61.
2. J. De Castro, H. Nogami, and J. Yagi: *ISIJ Int.*, 2001, vol. 41, pp. 18–24.
3. M. Chu, H. Nogami, and J. Yagi: *ISIJ Int.*, 2004, vol. 44, pp. 801–08.
4. H. Nogami, P. Austin, J. Yagi, and K. Yamaguchi: *ISIJ Int.*, 2004, vol. 44, pp. 500–09.

5. H. Nogami, H. Yamaoka, and K. Takatani: *ISIJ Int*., 2004, vol. 44, pp. 2150–58.
6. J. Castro, H. Nogami, and J. Yagi: *ISIJ Int*., 2000, vol. 40, pp. 637–46.
7. S. Natsui, T. Kikuchi, and R. Suzuki: *Metall. Mater. Trans. B*, 2014, vol. 45B, pp. 2395–2413.
8. S. Yuu, T. Umekage, S. Matsuzaki, M. Kadowaki, and K. Kunitomo: *ISIJ Int*., 2010, vol. 50, pp. 962–71.
9. X. Dong, A. Yu, S. Chew, and P. Zulli: *Metall. Mater. Trans. B*, 2010, vol. 41B, pp. 330–49.
10. J. Yagi: *ISIJ Int*., 1993, vol. 33, pp. 619–39.
11. X. Dong, A. Yu, J. Yagi, and P. Zulli: *ISIJ Int*., 2007, vol. 47, pp. 1553–70.
12. X. Dong, A.B. Yu, J. Burgess, D. Pinson, S. Chew, and P. Zulli: *Ind. Eng. Chem. Res*., 2009, vol. 48, pp. 214–26.
13. S. Zhang, A. Yu, P. Zulli, B. Wright, and P. Austin: *Appl. Math. Model*., 2002, vol. 26, pp. 141–54.
14. S. Story and R. Fruehan: *Metall. Mater. Trans. B*, 2000, vol. 31B, pp. 43–54.
15. M. Shin, S. Min, J. Lee, J. Park, and D. Min: *Met. Mater. Int*., 2012, vol. 18, pp. 1041–47.
16. M. Shin, J. Oh, and J. Lee: *ISIJ Int*., 2015, vol. 55, pp. 2056–63.
17. D. Jang, Y. Kim, M. Shin, and J. Lee: *Metall. Mater. Trans. B*, 2012, vol. 43B, pp. 1308–14.
18. H. Bertling: *ISIJ Int*., 1999, vol. 39, pp. 617–24.
19. Y. Kashihara, Y. Iwai, N. Ishiwata, N. Oyama, H. Matsuno, H. Horikoshi, K. Yamamoto, and M. Kuwabara: *ISIJ Int*., 2017, vol. 57, pp. 665–72.
20. Y. Kashihara, Y. Iwai, T. Sato, N. Ishiwata, and M. Sato: *ISIJ Int*., 2015, vol. 55, pp. 1237–44.
21. K. Ichikawa, Y. Kashihara, N. Oyama, T. Hirosawa, J. Ishii M. Sato, and H. Matsuno: *ISIJ Int*., 2017, vol. 57, pp. 254–61.
22. J. Chung and N. Hur: *ISIJ Int*., 1997, vol. 37, pp. 119–25.
23. K. Takahashi, T. Nouchi, M. Sato, and T. Ariyama: *ISIJ Int*., 2015, vol. 55, pp. 1866–75.
24. M. Sato, K. Takahashi, T. Nouchi, and T. Ariyama: *ISIJ Int*., 2015, vol. 55, pp. 2105–14.
25. H. Nogami, Y. Kashiwaya, and D. Yamada: *ISIJ Int*., 2012, vol. 52, pp. 1523–27.
26. J. Li, P. Wang, L. Zhou, and M. Cheng: *ISIJ Int*., 2007, vol. 47, pp. 1097–1101.
27. M. Geerdes, H. Toxopeus, and C. van der Vliet: *Modern Blast Furnace Ironmaking: An Introduction*, 2nd ed., IOS Press B.V, Amsterdam, 2009, pp. 67–92.
28. Z. Fan, S. Igarashi, S. Natsui, S. Ueda, T. Yang, R. Inoue, and T. Ariyama: *ISIJ Int*., 2010, vol. 50, pp. 1406–12.
29. K. Yang, S. Choi, J. Chung, and J. Yagi: *ISIJ Int*., 2010, vol. 50, pp. 972–80.
30. D. Fu, Y. Chen, Y. Zhao, J. D'Alessio, K. Ferron, and C. Zhou: *Appl. Therm. Eng*., 2014, vol. 66, pp. 298–308.
31. P. Cundall and O. Strack: *Geotechnique*, 1979, vol. 29, pp. 47–65.
32. J. Park, H. Jung, M. Jo, H. Oh, and J. Han: *Met. Mater. Int*., 2011, vol. 17, pp. 485–96.
33. Y. Tsuji, T. Kawaguchi, and T. Tanaka: *Powder Technol*., 1993, vol. 77, pp. 79–87.
34. Q. Hou, E. Dianyu, S. Kuang, Z. Li, and A.B. Yu: *Powder Technol*., 2017, vol. 314, pp. 557–66.
35. B. Xu, A.B. Yu, S.J. Chew, and P. Zulli: *Powder Technol*., 2000, vol. 109, pp. 13–26.
36. B.H. Xu and A.B. Yu: *Chem. Eng. Sci*., 1997, vol. 52, pp. 2785–2809.
37. S. Matsuhashi, H. Kurosawa, S. Natsui, T. Kon, S. Ueda, R. Inoue, and T. Ariyama: *ISIJ Int*., 2012, vol. 52, pp. 1990–99.
38. H. Zhu, Z. Zhou, A.B. Yu, and P. Zulli: *Granul. Matter*, 2009, vol. 11, pp. 269–80.
39. S. Natsui, S. Ueda, H. Nogami, J. Kano, R. Inoue, and T. Ariyama: *ISIJ Int*., 2011, vol. 51, pp. 1410–17.
40. T. Ariyama, S. Natsui, T. Kon, S. Ueda, S. Kikuchi, and H. Nogami: *ISIJ Int*., 2014, vol. 100, pp. 198–210.
41. S. Natsui, S. Ueda, H. Nogami, J. Kano, R. Inoue, and T. Ariyama: *ISIJ Int*., 2011, vol. 51, pp. 51–58.
42. S. Ueda, T. Kon, H. Kurosawa, S. Natsui, T. Ariyama, and H. Nogami: *ISIJ Int*., 2015, vol. 55, pp. 1232–36.
43. S. Natsui, H. Nogami, S. Ueda, J. Kano, R. Inoue, and T. Ariyama: *ISIJ Int*., 2011, vol. 51, pp. 41–50.
44. Z. Miao, Z. Zhou, A.B. Yu, and Y. Shen: *Powder Technol*., 2017, vol. 314, pp. 542–49.
45. H. Kurosawa, S. Matsuhashi, S. Natsui, T. Kon, S. Ueda, R. Inoue, and T. Ariyama: *ISIJ Int*., 2012, vol. 52, pp. 1010–17.
46. Z.Y. Zhou, H.P. Zhu, A.B. Yu, B. Wright, and P. Zulli: *Comput. Chem. Eng*., 2008, vol. 32, pp. 1760–72.
47. Z. Fan, S. Natsui, S. Ueda, T. Yang, J. Kano, R. Inoue, and T. Ariyama: *ISIJ Int*., 2010, vol. 50, pp. 946–53.
48. J. Zhang, Y. Chen, Z. Fan, Z. Hu, T. Yang, and T. Ariyama: *J. Iron Steel Res. Int*., 2011, vol. 18, pp. 1–6.
49. S. Natsui, S. Ueda, Z. Fan, N. Andersson, J. Kano, R. Inoue, and T. Ariyama: *ISIJ Int*., 2010, vol. 50, pp. 207–14.
50. S. Natsui, S. Ueda, M. Oikawa, Z. Fan, J. Kano, R. Inoue, and T. Ariyama: *ISIJ Int*., 2009, vol. 49, pp. 1308–15.
51. M. Keyser, M. Conradie, M. Coertzen, and J. Van Dyk: *Fuel*, 2006, vol. 85, pp. 1439–45.
52. T. Nouchi, T. Sato, M. Sato, K. Takeda, and T. Ariyama: *ISIJ Int*., 2005, vol. 45, pp. 1426–31.
53. Y. Yu, A. Westerlund, T. Paananen, and H. Saxen: *ISIJ Int*., 2011, vol. 51, pp. 1050–56.
54. Y. Yu and H. Saxen: *ISIJ Int*., 2012, vol. 52, pp. 788–96.
55. Z. Zhou, H. Zhu, A. Yu, B. Wright, D. Pinson, and P. Zulli: *ISIJ Int*., 2005, vol. 45, pp. 1828–37.
56. S. Kikuchi, T. Kon, S. Ueda, S. Natsui, R. Inoue, and T. Ariyama: *ISIJ Int*., 2015, vol. 55, pp. 1313–20.
57. F. Zhengyun, S. Natsui, S. Ueda, J. Kano, R. Inoue, and T. Ariyama: *Tetsu-to-Hagane*, 2010, vol. 96, pp. 1–10.
58. Y. Omori: *Blast Furnace Phenomena and Modelling*, Elsevier Applied Science Publishers, London, 1987, pp. 3–63.